



Large-Scale Surfactant Exfoliation of Graphene and Conductivity-Optimized Graphite Enabling Wireless Connectivity

Matthew J. Large,* Sean P. Ogilvie, Aline Amorim Graf, Peter J. Lynch, Marcus A. O'Mara, Thomas Waters, Izabela Jurewicz, Jonathan P. Salvage, and Alan B. Dalton*

Graphene and other graphitic materials are suggested as a route to cheap, high-performance, environmentally-sustainable electronic devices owing to their almost unique combination of properties. Liquid-phase exfoliation is a family of shear-based techniques that produce dispersions of nanosheets from bulk layered material crystallites. High-quality nanosheets of graphene can be produced in solvents or surfactant dispersions; however the lateral size of these sheets limits the network transport properties observed in printed films. A high-throughput, industrially-scalable aqueous process for the production of graphene and related layered nanomaterials is presented. By considering not only the exfoliation process, but also the size selection and deposition processes, printable graphitic nanoparticulate materials with conductivities up to $50\,000\text{ S m}^{-1}$ are demonstrated. This value is ten times larger than is typically obtained for few-layer graphene produced by liquid-phase exfoliation. The size selection process is critical to obtaining the maximum conductivity of deposited films, with an optimized nanographite having greater performance than few-layer graphene or graphite that is processed and used without size selection. Building on these results a radio-frequency antenna application is demonstrated, which is competitive with the state-of-the-art, and a route to recycling of such printed short-life-time electronic devices to lower the environmental impact is discussed.

of properties. High electrical conductivity, mechanical flexibility, and a wealth of different processing routes make it an ideal prospect in many diverse application areas, such as printable circuits or ubiquitous Internet of Things (IoT) devices. One of the main roadblocks, however, is that the processes by which the largest volumes of material may be produced—including liquid-phase exfoliation, or LPE, and chemical and electrochemical exfoliation—tend to result in lower electronic performance. LPE is a family of shear-based techniques that produce dispersions of nanosheets from bulk layered material crystallites.^[1] High-quality nanosheets of graphene can be produced in solvents or surfactant-water dispersions; however the lateral size of these sheets places limitations on the network transport properties observed in subsequently-deposited thin films. Chemical and electrochemical exfoliation routes, on the other hand, tend to produce large sheets which have a high density of basal plane defects. These defects

1. Introduction

Graphene materials have long been suggested as a route to cheap, high-performance, environmentally-sustainable electronic devices owing to their almost unique combination

hinder transport performance unless repaired through aggressive processes such as high-temperature annealing or chemical post-treatment.^[2,3]

Routes to production of LPE nanosheets include ultrasonication,^[1,4] high-shear rotary mixing,^[5] and high-pressure homogenization (also variously referred to as wet-jet milling or microfluidization depending on the specific equipment employed).^[6–8] Each of these techniques produces a broad distribution of particle thicknesses and lateral sizes in dispersion, that may be subsequently size-selected to yield dispersions of controlled particle distribution (e.g., centrifugation or filtration) if required.

In order for these LPE graphene materials to represent viable competition to metallic conductors in future electronic applications—such as elements of distributed IoT systems—three principal considerations must be met; 1) the process for production must be scalable, 2) to minimize environmental impacts, the process should use “green” carrier liquids and minimal process energy, 3) a high conductivity is required in the deposited films. Deposition of these materials at industrial scale is likely to be via various printing techniques, as these additive manufacturing processes are highly adaptable. As such, in practical terms film thicknesses are limited to those achievable by printing technologies (broadly in the range up

Dr. M. J. Large, Dr. S. P. Ogilvie, A. Amorim Graf, Dr. P. J. Lynch, M. A. O'Mara, Prof. A. B. Dalton

University of Sussex
Brighton BN1 9RH, UK

E-mail: m.large@sussex.ac.uk; a.b.dalton@sussex.ac.uk

T. Waters, Dr. I. Jurewicz
University of Sussex
Guildford GU2 7XH, UK

Dr. J. P. Salvage
University of Brighton
Brighton BN2 4HP, UK

 The ORCID identification number(s) for the author(s) of this article can be found under <https://doi.org/10.1002/admt.202000284>.

© 2020 The Authors. Published by WILEY-VCH Verlag GmbH & Co. KGaA, Weinheim. This is an open access article under the terms of the Creative Commons Attribution License, which permits use, distribution and reproduction in any medium, provided the original work is properly cited.

DOI: 10.1002/admt.202000284

to 20 μm). If we place an upper bound on the sheet resistance of 1 Ohm sq^{-1} at these printable thicknesses, the minimum conductivity required of these materials (per consideration (3) above) is 50 000 S m^{-1} . As a point of reference, pristine monocrystalline graphite has a conductivity of $>2 \times 10^6 \text{ S m}^{-1}$,^[9] and would require a film thickness of $\approx 400 \text{ nm}$ to achieve this sheet resistance (even though such a system cannot be printed).

In this work, we have developed a high-throughput, industrially-scalable liquid-phase process for the production of graphene and related layered nanomaterials, meeting the considerations (1)–(3) discussed above. By considering not only the exfoliation process, but also the size selection process, we are able to demonstrate graphitic nanoparticulate materials with conductivities up to 50 000 S m^{-1} . This value is around one order of magnitude larger than is often obtained for few-layer graphene produced by LPE processes, with the added benefit of a water–surfactant process with no subsequent washing or annealing. We find that the size selection process is critical to obtain the maximum conductivity of deposited films, with our conductivity-optimized graphite (COG) having greater performance than few-layer graphene or graphite that is processed and used without size selection (as is the case in other work).

Utilizing our optimized COG material we demonstrate a RFID antenna which is competitive with the state-of-the-art and enables possibilities for all-printed radio communication devices. We show how such printed electronic devices may be recycled to lower the environmental impact of future generations of single-use and short-lifetime electronics, as are to be anticipated with the expansion of the Internet of Things.

2. Results and Discussion

In this work we utilize high-pressure homogenization equipment, illustrated schematically in **Figure 1A**. The system features a hydraulic system (not shown) that drives an intensifier pump to generate pressures up to 3000 atm on the process side. The compressed process fluid is then depressurized through a diamond nozzle within the process cell, producing a high velocity jet which impinges on fluid flowing in the reverse direction within the cell. This process generates turbulent shear forces which are responsible for delamination of the bulk crystallites, ultimately leading to exfoliation of layered materials into few-layer nanosheets. The pilot-scale machine shown in **Figure 1A** is capable of flow rates up to 20 L h^{-1} , where the use of recirculation of the working fluid reduces the throughput to $20/N \text{ L h}^{-1}$, where N is the number of passes of the fluid through the process.

To demonstrate that this equipment is capable of exfoliating layered nanomaterials into few-layer nanosheets, graphite powder was processed and subsequently size-selected by centrifugation so as to retain only the few-layer nanosheets of graphene produced.^[10] Whereas other work utilizes flake graphite,^[5,11] in this work we use fine powders with 1–50 μm flake sizes produced by air classification of milled powder. This is necessary because the typical particle sizes in flake graphite are larger than the diameter of the process nozzle (ca 100 μm).

The graphite is dispersed into a surfactant–water system and added to the inlet reservoir (see **Figure 1A**), from where it is

drawn into the intensifier pump on each piston back stroke. The fluid is then pressurized and accelerated under decompression (as discussed above) before exiting the process cell into a heat exchanger. This is done because the turbulent dissipation of energy generates a significant amount of heat within the system; approximately 1.5 $^{\circ}\text{C}$ for each 1 kPSI increase in operating pressure. Once the fluid is cooled to a temperature maintained by an external chiller system, it is either collected or recirculated, depending on the system configuration.

Once the graphite has been processed, we centrifuge at 5000 g for 20 min to remove all unexfoliated crystallites and larger fragments; this combination of parameters, based on our previous work,^[10] is expected to sediment all but the few-layer nanosheets present. **Figure 1B** (and the associated inset) illustrates the graphitic particles produced by this process. Nanosheets of graphene are obtained with a distribution of lateral sizes and thicknesses ranging from 50 to 800 nm and up to $\approx 20 \text{ nm}$, respectively. We note that this likely corresponds to particles up to 20 layers thick, given that the measured interlayer spacing of graphene produced by liquid exfoliation is $\approx 1 \text{ nm}$,^[5] which is significantly higher than expected for pristine or bulk graphite (0.34 nm). As such we anticipate approximately half of the nanosheets present are few-layer graphene (<10 layers).

In order to assess the population properties of the dispersions produced by such a process, we utilize UV–vis spectrophotometry as illustrated in **Figure 1C** (with the associated metric inset)^[12] to evaluate the average layer number of nanosheet populations. The spectra for the three fractions shown have been obtained by varying the product of the relative centrifugal force (RCF) and centrifugation time to select different portions of the as-produced nanosheet population. Additionally, the inset photograph shows that we are able to process most other layered nanomaterials in the same way; yielding few-layer dispersions of molybdenum disulfide, tungsten disulfide, hexagonal boron nitride, molybdenum diselenide, and tungsten diselenide at similarly large scales.

With the fundamental process demonstrated, **Figure 1D–F** illustrate how the yield of few-layer graphene varies as a function of available process parameters, including number of recirculation passes, operating pressure, and chiller operating temperature. In **Figure 1D** we observe an approximately square root dependence of the yield (calculated as the ratio of few-layer graphene concentration after centrifugation to the initial graphite concentration) on the number of passes of the dispersion through the system for a fixed operating pressure and chiller operating temperature. This has a direct analogue in other LPE processes such as sonication and high-shear mixing, where similar dependence of the final concentration on processing time are observed.^[5,11] The inset plot of average layer number shows a very rapid decrease between one and five passes, after which the dispersion quality stabilizes. A power law fit is shown as a guide to the eye.

Figure 1E shows the dependence of few-layer graphene yield against the process pressure where the number of passes and chiller temperature are fixed. Here we see that the yield increases super-linearly according to a power law with exponent ≈ 1.8 . The inset plot of layer number, with a fitted power law for consistency with the inset in **Figure 1D**, shows a minor

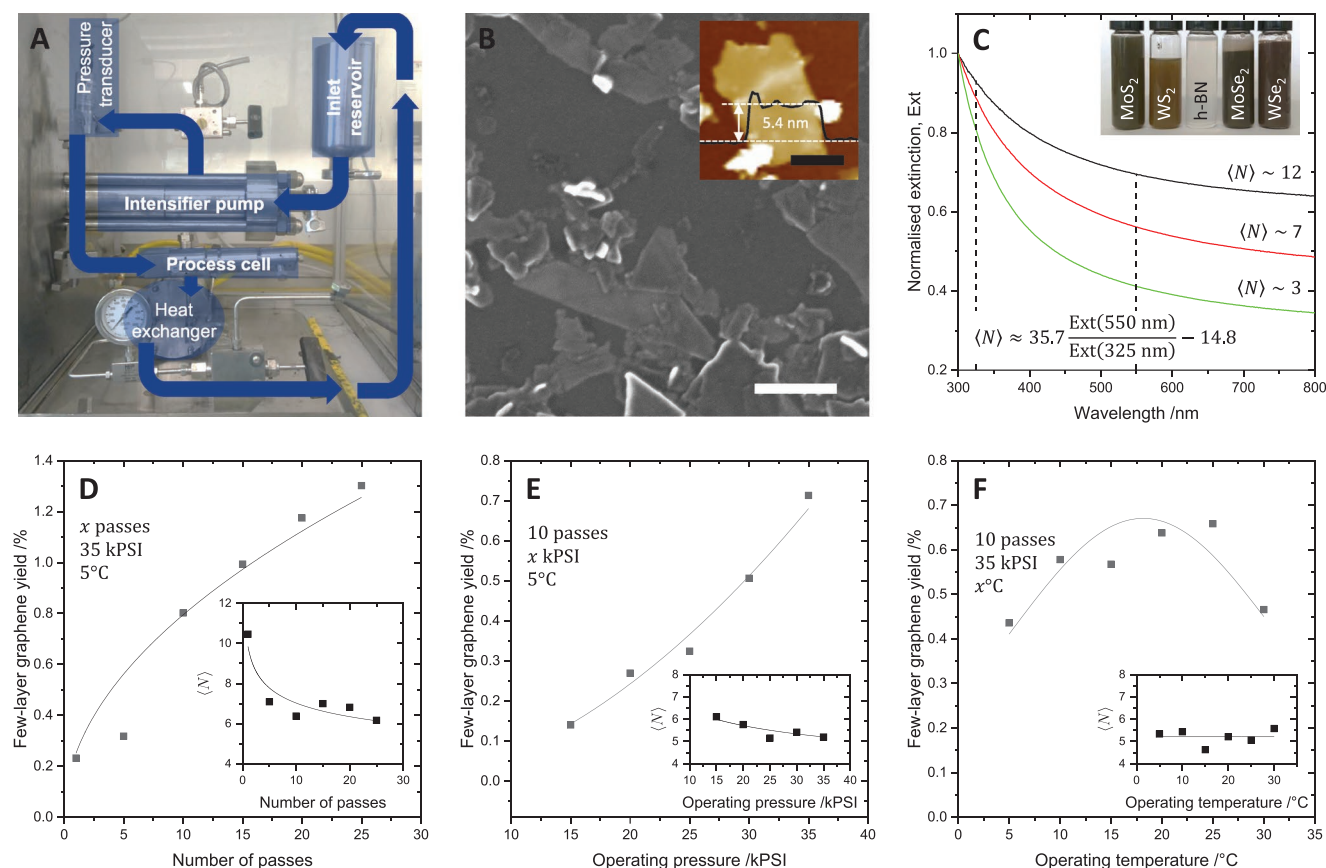


Figure 1. A) Schematic of the high-pressure homogenization equipment employed in this study, overlaid on a photograph of the system. The flow of fluid is indicated by arrows between the system components. B) Scanning electron micrograph (scale bar 400 nm) and inset atomic force micrograph (scale bar 200 nm) illustrating the presence of graphene nanosheets in material processed using the equipment in (A). Also see Figure S1, Supporting Information for associated Raman analysis. (inset) AFM topography of a few-layer nanosheet. C) UV-vis spectroscopy of three centrifugation-selected fractions illustrating a change in the average layer number of the dispersed nanosheets. (inset) Images of few-layer dispersions of other layered nanomaterials prepared using the same process. D) Plot of graphene yield against the number of recirculation passes of the dispersion through the equipment. E) Plot of the graphene yield against the fluid operating pressure generated by the intensifier pump. (inset) Average layer number of the dispersion against operating pressure. F) Plot of graphene yield against chiller operating temperature. (inset) Average layer number against chiller operating temperature.

decrease in average layer number with increasing pressure; this suggests, as the yield data does, that the quality of exfoliation improves with increasing pressure. Indeed, the operating pressure influences both the flow rate and acceleration of fluid at the process nozzle, and thereby influences the turbulent and shear forces that act on the crystallites during exfoliation. Figure 1F plots the equivalent yield data against the chiller operating temperature, at fixed pressure and number of passes. Interestingly, we observe a non-monotonic behavior, fitted with a Gaussian function, which has a maximum between 15 and 20 °C. Given that there is a significant temperature rise above this within the system (as a result of turbulent energy dissipation discussed above) we estimate that the optimum fluid temperature inside the process cell may be in the region of 65 to 75 °C. The equivalent inset plot of average layer number to those in Figure 1D,E shows no dependence on the chiller temperature; the fitted power law has an optimized exponent of ≈ 0 .

There are multiple contributing factors to the temperature effect on the process yield that may lead to the appearance

of an optimum. For example, the surface energy of the fluid (water-surfactant solution) will decrease as the temperature increases; there is existing evidence to suggest that an optimum temperature exists due to this effect based on ultrasonication experiments.^[13] Adsorption and desorption kinetics of surfactant molecules will also vary with temperature, plausibly resulting in a change in equilibrium surface coverage of surfactant molecules on the nanomaterial surface affecting dispersion stability. Additionally, other physical properties of the solvent, such as viscosity, which affect the induced shear rate and therefore the ultimate process yield.

While the experiments in Figure 1 do not necessarily constitute a full optimization of the exfoliation process (since it is likely that the effects of multiple parameters on the exfoliation yield are interdependent), these data illustrate the influence of important process parameters which will inform scale-up of the process to industrial capacity in a fashion similar to previous large-scale techniques.^[15] Even considering the pilot scale equipment employed in this work, the yield and throughput for optimized process parameters suggest that 0.5 g h⁻¹ of few-layer

graphene can be produced at the lab scale; equivalent to almost 5 kg of graphene nanoplatelets per year.

One issue that affects the applications integration of few-layer graphene is that deposited films have a conductivity significantly below the threshold set in the discussion above. This is partially a result of significant quantities of adsorbed surfactant or other residues, owing to the high specific surface area of exfoliated nanosheets. In a typical ultrasonication-based method the starting composition is often around 5:1 in terms of the bulk material powder to surfactant (by weight). Given that exfoliation yields of few-layer materials are typically around 1%, this means that the final surfactant content (after removal of unexfoliated material) is in the region of 1:20 nanosheets to surfactant by weight. It is this anecdotal consideration that gives rise to the perception that “surfactant-exfoliated graphene films are not conductive”. Additionally, the small lateral sheet size increases the density of junctions within a film, which contribute centers for charge scattering thereby lowering the network conductivity. Both of these considerations would suggest that selecting larger multilayers should yield a higher

conductivity in the final deposited films; both for a lower specific surface area (which scales reciprocally with layer number), and a larger lateral sheet size that comes with a well-defined scaling behavior between layer number and aspect ratio of the nanosheets.^[14]

Figure 2 summarizes the results of a series of size selection experiments intended to elucidate the effect of centrifugation on the as-produced population of nanosheets within the homogenized dispersions. As a result of starting with a fine graphite powder, the homogenization process produces a very broad distribution of particles from unexfoliated crystallites to few-layer nanosheets. This is in contrast to work where flake graphite is used, where the distribution is generally bimodal, with a contribution from the exfoliated material and one from the unexfoliated material (which can be removed using very low RCF-time products due to the large particle size).

Figure 2A shows both the average layer number (from UV-vis) and average lateral sheet size (from dynamic light scattering (DLS) per the metric established elsewhere in the literature)^[15] as a function of RCF-time product over a broad

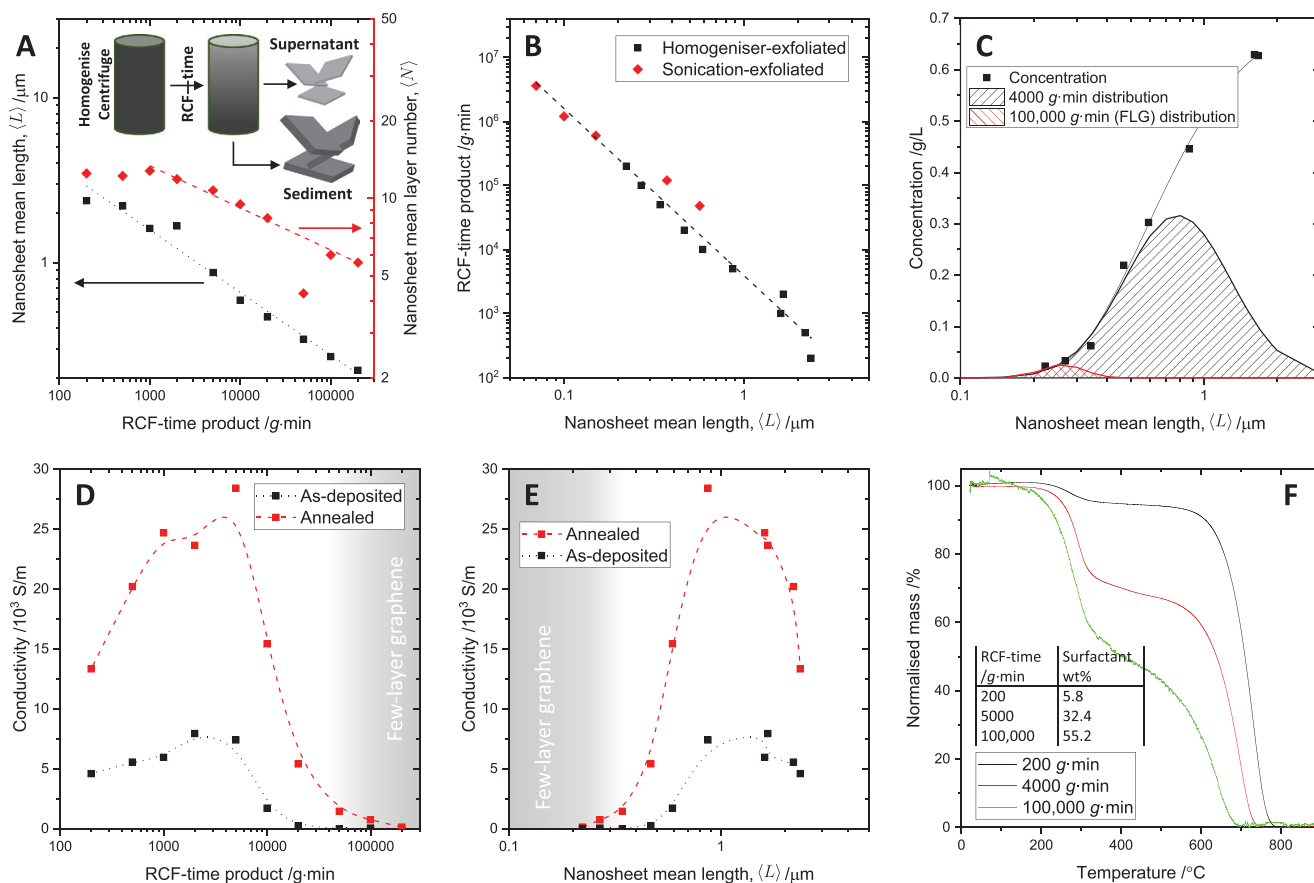


Figure 2. A) Plot of nanosheet mean length (left axis) and nanosheet mean layer number (right axis) as a function of RCF-time product for a single step centrifugation process (illustrated in the inset). B) Scaling relationship between the RCF-time product and selected mean nanosheet length, showing consistency between ultrasonic exfoliation of graphene and the present homogenization process. C) Reconstructed particle size distribution based on the lateral size measurements in (A) and the corresponding sample concentrations (see Figure S2, Supporting Information). Shown are schematic distributions to illustrate the effect of low and high RCF-time product size selections. D,E) Plots of film conductivity before and after annealing as a function of RCF-time product and nanosheet mean length, respectively. (The data are replotted on a log–log scale in Figure S3, Supporting Information) F) Thermogravimetric analysis of three size selected fractions illustrating the trend in surfactant content with decreasing average layer number of the dispersions.

range. The inset schematic illustrates that a single centrifugation step is used, with the supernatant collected (corresponding to the samples measured) and the sediment discarded. At the lowest end, the RCF-time product is accessible through simple standing of dispersions at 1 g for a matter of hours, whereas at the highest end of the range the sedimentation times would be in the range of months. We observe, as in our prior work,^[10] a power law relationship between both (L) and (N) in terms of the RCF-time product. Figure 2B compares the scaling observed for the homogenized material with that data from ultrasonic exfoliation from flake graphite. It is clear that both data series can be fitted accurately with a single power law, indicating that the population of particles produced by homogenization is self-similar in the same fashion as that produced by sonication; this gives us indicative support for the idea that homogenization does indeed exfoliate graphite by a similar microscopic process as has been utilized in other work.

Utilizing the size selection parameters as well as the measured concentrations for each of the fractions analyzed in Figure 2A,B we are able to reconstruct the stock nanosheet population in terms of lateral sheet size, as shown in Figure 1C. The data are fitted with one tail of a lognormal distribution as a guide to the eye; given there are no data points on the other tail of the distribution, it is difficult to assess the precise distribution function. Measurements at lower RCF-time product which would produce information in this range are challenging as the sedimentation times for dispersions approach the UV-vis and DLS measurement times. Beneath the population distribution curve we show a pair of schematic distributions approximately representing the few-layer graphene distribution (selected at 100 000 g-min centrifugation) as compared to a broader distribution of thicker material selected at 4000 g-min. What we see is that the larger fraction has an area of approximately 10 \times that of the few-layer graphene distribution, suggesting that judicious selection of the nanosheet size based on the functional performance may give higher mass yields, production rates, and lower specific energy consumptions. By way of example, the production of few-layer graphene using this pilot equipment requires a specific energy consumption of the order of 100 MJ g⁻¹; by optimization of the size-selection approach there is the prospect of lowering this by at least an order of magnitude. Further savings are available through economies of scale, potentially allowing nanomaterials to reach cost parity with metals such as aluminum.

To this end, we spray coated the size selected dispersions to measure the film conductivity. The data are presented as a function of the RCF-time product in Figure 2D and as a function of the lateral sheet size in Figure 2E. In order to isolate the effects of surfactant content and sheet size effects, the film conductivities were measured (using the transmission line method) before and after annealing of the films at 300 °C for 10 min to drive off the surfactant. The surfactant used (Triton X-100) is a liquid at room temperature with a boiling point of \approx 270 °C, so annealing of the films results in evaporation of the surfactant from the structure, rather than carbonization as is observed in other works where solid surfactants or polymers are used,^[16] or where solvent residues are present. Elimination of the surfactant in this way reduces inter-sheet junction resistances, and thereby increases the film conductivity. Spray deposition,

as with all printing processes, retains all residue present in the dispersions, whereas processes such as vacuum filtration inherently wash the samples to some degree even though this is not always acknowledged. This highlights the need for low-residue dispersions for any large-scale printing applications, especially where thermal post-treatments are not possible.

From the fractions with the most selection (highest RCF-time product) we observe an increase in conductivity with decreasing RCF-time product up to a maximum situated between 2000 and 5000 g-min; from Figure 2E this corresponds to a nanosheet lateral size of \approx 1 μ m on average. The approximate length distribution of this fraction is that schematically shown in Figure 1C for a 4000 g-min RCF-time product. Moving from high to lower RCF-time product corresponds to including progressively larger nanosheets in the supernatant dispersion after centrifugation. The maximum conductivity obtained without annealing is \approx 8000 S m⁻¹. However, as we continue to lower the RCF-time product the conductivity begins to fall down to 4000 S m⁻¹ at 200 g-min centrifugation. Figure S3, Supporting Information replots the data from Figure 2D,E on logarithmic y-scales and shows a power law fit to the high-RCF-time side of the data.

After annealing of the films, a significant increase in conductivity is observed; Figure S4, Supporting Information. At low values of the RCF-time product the conductivity ratio varies between a factor of 3 and 4 increase after annealing. However for increasing RCF-time product the conductivity ratio increases in an approximately power law fashion over several orders of magnitude. This indicates that the surfactant content of the highly-exfoliated material increases as the degree of exfoliation improves, as demonstrated by the thermogravimetric analysis (TGA) shown in Figure 2F. We can also infer that for the largest nanosheets, the surfactant content is not the limiting factor affecting the network conductivity. It is likely that effects of porosity and alignment of the nanosheets (which influences the inter-nanosheet junction resistance) play a role. Additionally, the post-annealing conductivity for RCF-time products greater than the optimum exhibit a power law scaling that is indicative of variation in the nanosheet length with centrifugation conditions (as plotted in Figure 2B).

The maximum conductivity obtained by annealing is \approx 28 000 S m⁻¹, which is approaching the threshold conductivity set in the introductory section of this article. This conductivity-optimized graphite (COG) material appears to have properties determined by the competing influences of multiple effects; the balance of lateral nanosheet length and residue content for smaller thinner nanosheets, and alignment and film porosity for larger thicker nanosheets.

While the process of post-deposition annealing is instructive in understanding the effects of residue content on film conductivity, there are several practical issues that prevent such a step forming part of any scalable industrial manufacturing approach. As discussed, not all surfactants are volatile and carbonize under elevated temperature; similarly, many flexible polymer-based substrates are unable to withstand extremes in temperature. As such, we consider calendaring^[17–20] as an alternative low-temperature roll-to-roll process which reduces porosity and increases nanosheet alignment.

Figure 3A shows measurements of a representative sample before and after compression by calendaring; as can be seen

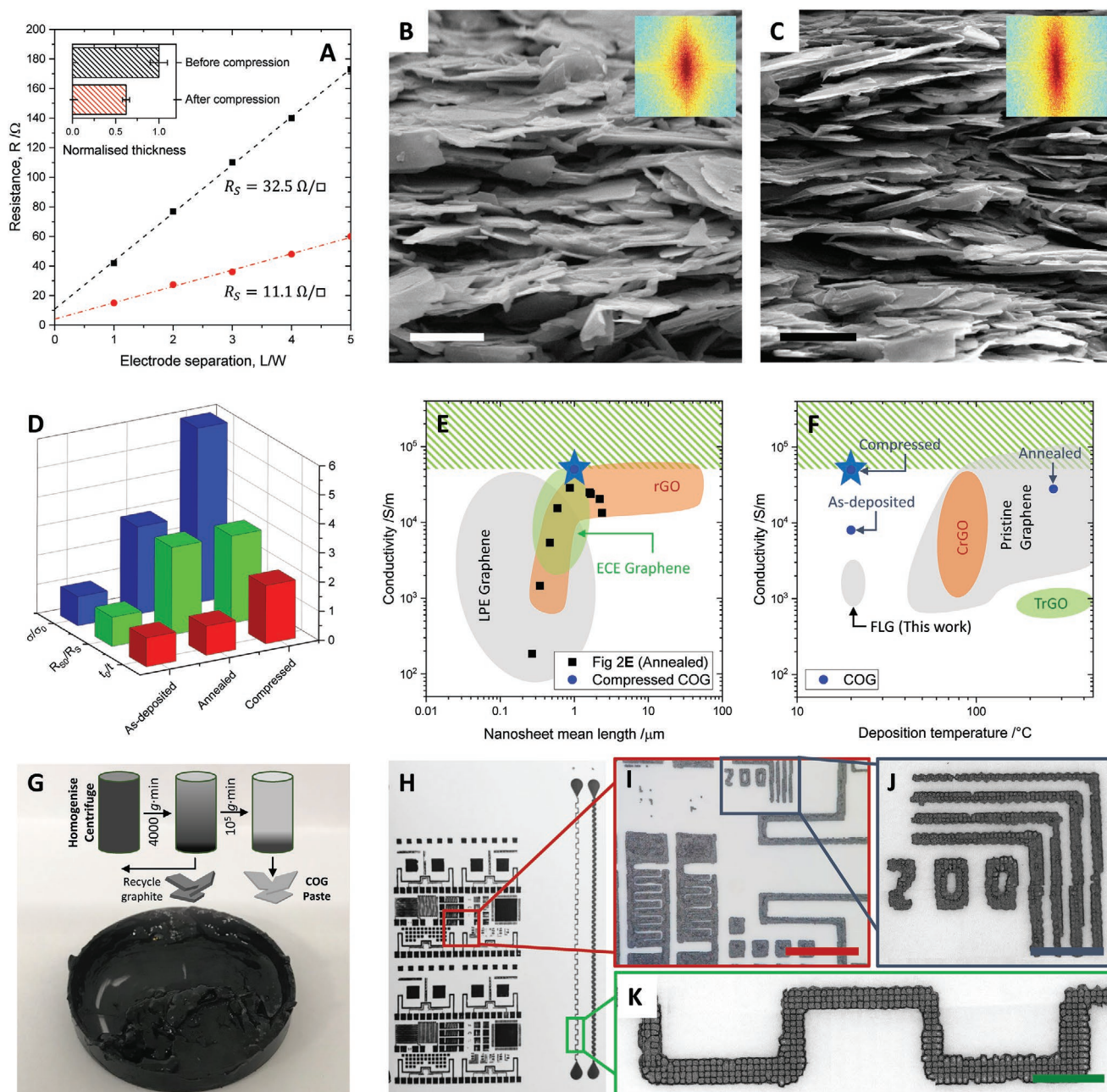


Figure 3. A) Resistance versus normalized electrode separation from transmission line measurements of sheet resistance for a printed COG film before and after calendaring. (inset) film thickness before and after calendaring. B,C) Scanning electron micrographs of film cross sections before and after calendaring (respectively). The scale bars are 1 μm . (insets) Fast Fourier transform (FFT) analysis of the images indicates an increase in horizontal nanosheet alignment after calendaring. D) Bar chart illustrating the approximate relative influences of various processes on the ratio of film thickness ratios, sheet resistance ratios, and conductivity ratios before and after each process. E) Bubble plot showing realized conductivities for graphene-based materials against nanosheet mean length, modified from.^[12] F) Bubble plot showing realized conductivities for graphene-based materials against deposition temperature, modified from.^[16] G) Image of centrifugation-produced COG paste with inset production schematic. H) Photograph of an uncalendered screen printed test pattern using the paste shown in (G). I–K) Micrographs at varying magnifications of areas of the sample in (H). Scale bars are 2.5, 1, and 1 mm, respectively.

there is a reduction in film thickness of approximately a factor of two, and an associated decrease in sheet resistance of approximately a factor of three. The combination of these two changes means that the film conductivity increases by a factor of ≈ 6 from 8000 S m^{-1} to approximately $50\,000 \text{ S m}^{-1}$. Figure 3B,C

show scanning electron micrographs of fracture cross-sections for the film before and after compression, respectively. While the spray deposition used in this case produces a relatively high degree of alignment (as visible in Figure 3B) the inset Fourier transforms of the SEM images indicates an increase in the

degree of alignment of the nanosheets after calendaring. Figure S5, Supporting Information additionally shows lower magnification images of the cross-sections, with the thicknesses highlighted as a guide to the eye, emphasizing that the calendaring reduces the film thickness by approximately a factor of two.

By comparison to the annealing process described by Figure 2, we can begin to isolate contributions to the conductivity increase observed; these effects are illustrated in Figure 3D. If we consider the compression ratio t_0/t (where t_0 and t are the initial and final film thicknesses, respectively) then we see that calendaring is the only process which produces a modification; approximately a factor of two, where direct deposition and annealing have values of unity. Second, the sheet resistance ratio R_{s0}/R_s (where R_{s0} and R_s are the initial and final sheet resistances, respectively) shows a similar value for both annealing and calendaring. The conductivity ratio is the product of these two previous ratios, since $\sigma = 1/(R_s t)$, and as noted the calendaring process shows the highest total improvement. We speculate that the sheet resistance change in the cases of calendaring and annealing are both the result of the removal of surfactant from the system; in the case of annealing this is by evaporation (as discussed), whereas in the case of calendaring the surfactant is displaced due to the compression of the film (since the surfactant is a liquid at room temperature).

Figure 3E,F compare the results from this work in terms of film conductivity with data modified from the literature,^[2,16] as functions of nanosheet lateral size and maximum process temperature, respectively. We find that our COG material competes favorably with other graphene-based materials in Figure 3E despite having a relatively low nanosheet length. Figure 3F shows that the calender-compressed COG films, deposited at room temperature, match the performance of other materials which necessitate processing at >80 °C, making the material highly competitive from a scale manufacturing point of view. As clearly illustrated in Figure 3E,F the materials discussed in this paper (including few-layer graphene and COG) have comparable conductivities to other materials, none of which are processed in surfactant.^[2,16] This directly contradicts the accepted wisdom that the use of surfactant-based processing for electronic applications is untenable due to the detrimental effects of residue content on film performance.

To move towards a more viable printing process than spray deposition, a high-solids-content paste of the COG material is produced through centrifugation,^[21] as illustrated schematically and in the photograph of Figure 3G. After the initial size selection step, the COG dispersions were centrifuged for 100 000 g·min (as would be used to select a few-layer graphene dispersion) causing the COG material to be sedimented. The resulting paste has a solids content of ≈ 30 wt.%, which can be let down to a suitable consistency for screen printing using a higher boiling point, water-miscible solvent (such as ethylene glycol) at a mass ratio of approximately 1:1. A comparison of thermogravimetric curves for the as-produced COG dispersion and COG paste is given in Figure S6, Supporting Information. Figure 3H–I shows images at multiple magnifications of a printed test pattern produced using the paste in Figure 3G onto high gloss photographic paper.

The feature of the design shown in Figure 3I and magnified in Figure 3J is a series of 200 μm wide bars separated

by 200 μm gaps. The width of the inter-print gaps varies between 120 and 220 μm , with an average of 170 μm ; this indicates that there is up to 40 μm of “bleeding” of the ink out from the edges of the screen pattern. In turn, we estimate that the smallest reliably printable feature using this approach would be ≈ 100 μm . The track feature magnified in Figure 3K has a printed width of between 290 and 400 μm , with an average of 320 μm ; with a designed track width of 300 μm , this similarly suggests a degree of bleeding of the ink over the substrate.

Based on the materials performance and printing demonstrated above, Figure 4 investigates the use of COG materials in the preparation of ultra-high frequency (UHF) radio frequency identification (RFID) antennas and tags. In Figure 4A experimental return loss spectra (measured using a vector network analyzer, or VNA) are compared to a simulated spectrum for an original antenna design. As can be seen, the resonant feature of the antenna prepared exactly according to the simulated design is at a lower frequency than required, which is indicative of excessive capacitive damping. To combat this, the design was modified by reducing the area of the capacitive “wings” symmetrically on either side of the antenna, with the optimized antenna having a center frequency very closely matching that of the simulation. These results are compared to a commercially available aluminum antenna in Figure 4B. The apparent baseline offset of the COG antenna data relative to the aluminum antenna is due to closer matching of the COG antenna impedance to the VNA probe. The important feature is the relative depth of the resonant feature to the baseline in each case.

To assess the performance of the COG antenna in a practical RFID system we attached an Alien Higgs 3 RFID integrated circuit using a small aluminum support, as shown in Figure 4C. The resulting performance of the completed tag is assessed in Figure 4D,E. Figure 4D summarizes the results of a margin test performed with an Impinj Speedway Revolution R120 fixed RFID reader, whereby the transmitter power is progressively incremented at a given read distance until the tag is successfully read. The data indicates, given that the maximum transmitter power is 30 dBm, that the practical read distance is ≈ 2 m. However, the data presented in Figure 4E provides additional insight. The returned power from the tag is measured at the reader, and can be modeled using a simple link budget equation as in Equation (1).

$$P_R = P_{Tx} + G_{Tag} - FSPL + G_{Rx} - L_{add} \quad (1)$$

where P_R is the received power (in dBm) at the reader; P_{Tx} is the power transmitted by the RFID chip (-20 dBm from the datasheet); G_{Tag} is the gain of the tag antenna (1.8 to 2.0 dBi from simulation results); $FSPL = 20 \log(f_{read} d) - 27.55$ dB is the free space path loss (where $f_{read} = 867$ MHz is the reader carrier frequency, and d is the read distance in metres); G_{Rx} is the gain of the reader antenna (8.5 dBi from datasheet). The term L_{add} is an additional loss parameter that is added to allow the model to be fitted to the experimental data in Figure 4E, as shown. The fitted value of $L_{add} = 7.7$ dB, which may include contributions from antenna-IC impedance mismatch as well as any unassessed losses in the reader antenna

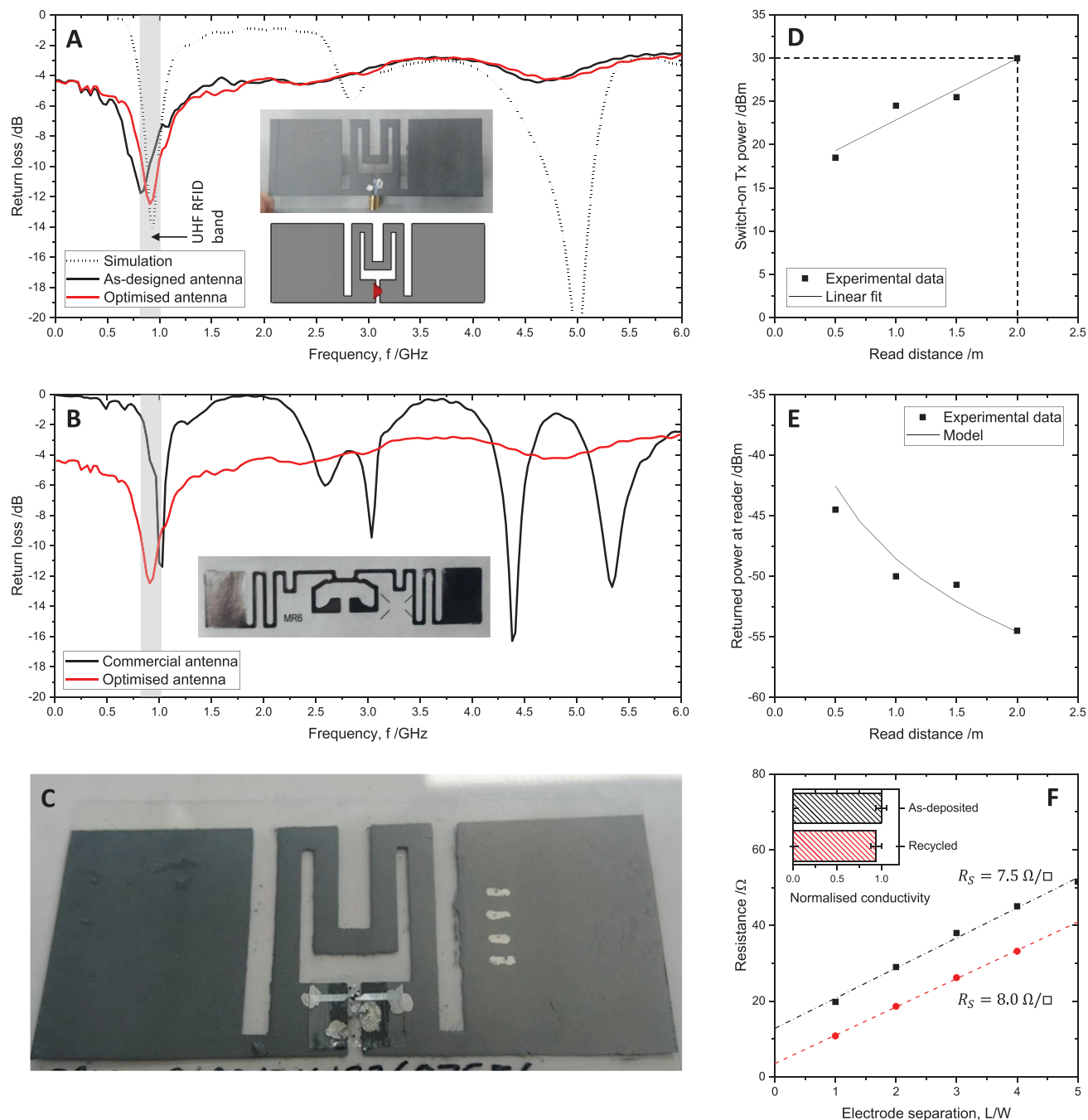


Figure 4. A) Comparison of simulated and measured return loss spectra for an ultra-high frequency (UHF) radio frequency identification (RFID) antenna. The shaded area represents the UHF band assigned to RFID covering both EU and USA territories.^[22] (inset) Images comparing the simulated geometry and realized antenna, fitted with a gold-plated SMA connector. B) Comparison of measured responses of the experimentally-optimized antenna from this work with a commercially-available aluminum antenna (shown in inset). Again, the UHF RFID frequency band is highlighted. C) Photograph of a RFID tag realized on PET by attachment of an Alien Higgs 3 IC. D) Results of a margin test, measuring the transmitter power that causes the tag in (C) to respond as a function of tag-reader distance in a noisy laboratory environment. E) Measurements of the returned power detected by the reader as a function of distance. F) Measurements demonstrated recyclability of the printed antenna; sheet resistance measurements of the as-prepared tag and after recycling (see Supporting Information) and redeposition. (inset) normalized conductivities, showing only a 6% decrease as a result of recycling of the antenna.

cable or resistive losses in the tag antenna itself. This also includes any deviations of the antenna gains from their estimated values.

Importantly, Equation (1) can be inverted to assess the theoretical maximum read distance of the tag based on the reader sensitivity (-70 dBm), as in Equation (2) below.

$$d_{\max} = \frac{1}{f_{\text{read}}} 10^{\left[\frac{P_{R,\min} - P_{Tx} - G_{\text{tag}} + 27.55 - G_{Rx} + L_{\text{add}}}{20} \right]} \quad (2)$$

The resulting value for the maximum read distance is $d_{\max} = 11.8$ m; this process eliminates issues with measurement of low return signals in a noisy RF environment (such as was used for these measurements) without requiring measurements to be performed in an anechoic chamber. Indeed, we note that the aluminum-based commercial tag, in our lab, can only be read to a distance of ≈ 3 m during a similar margin test to that in Figure 4D, despite a design specification of a minimum 10 m read range. This justifies our approach to assessment of the present tag antenna, and as such it can be seen that this tag is, in principle, competitive with other carbon-based antennas reported in the literature.^[19]

An additional point to note is that since these antennas are produced using a surfactant-exfoliated material with no washing, the COG may be redispersed from the substrate as a route to recycling. Currently hundreds of billions of RFID tags are produced annually, which are mostly single use and treated as disposable and therefore quickly end up in landfills. To demonstrate this recyclability, antenna fragments were redispersed into DI water (with no additional surfactant) by ultrasonication before being recoated. The film sheet resistance and conductivity before and after the recycling process are shown in Figure 4F. As evidenced, the conductivity of the recycled film meets that of the original antenna within the margin of error in the measurement, with only a 6% fall in the average value. The Supporting Information includes a short video showing the procedure used to recycle the antenna into an ink for re-use.

3. Conclusion

In the paper we have demonstrated and verified a high-throughput process for exfoliation of layered nanomaterials in an aqueous surfactant carrier. We have been able to achieve film conductivities of up to $50\,000$ S m^{-1} be a combination of optimized size-selection, deposition, and post-treatment procedures.

It is generally acknowledged that surfactant exfoliation is inappropriate for electronic applications since the residue content of deposited films severely hinders their performance. In a typical ultrasonication-based method the starting composition is often around 5:1 in terms of the bulk material powder to surfactant (by weight). Given that exfoliation yields of few-layer materials are typically around 1%, this means that the final surfactant content (after removal of unexfoliated material) is in the region of 1:20 nanosheets to surfactant by weight. It is this anecdotal consideration that gives rise to the perception that “surfactant-exfoliated graphene films are not conductive”. However, by reducing the initial surfactant ratio to 15:1, as in this work, and post-annealing films it is possible to realize conductivities over 1000 S m^{-1} .

By extension, we have demonstrated that size selection of larger, thicker nanosheets has the benefit of a lower surfactant content (due to lower specific surface area), and that these materials exhibit higher network conductivities due to a lower density of inter-nanosheet junctions as well as lower junction resistances (due to inherently larger overlap areas).

The multiple competing influences of nanosheet lateral size, surfactant residue, film porosity, and nanosheet alignment lead to an observed maximum in film conductivity for appropriate size selection procedures. This demonstrates that higher performance can be achieved with careful size-selection than is possible by either using only few-layer material, or without any size selection (as is common in other large-scale production work).^[6,8]

Elimination of film porosity and improving nanosheet alignment by calendaring yields significant gains in film conductivity, and is a significantly more practical approach than high-temperature annealing to reduce surfactant content in coated films.

Finally, we have demonstrated that achieving conductivities of $>50\,000$ S m^{-1} facilitates printing of films with sheet resistances of the order of 1 Ω sq^{-1} , and that this in turn facilitates the production of state-of-the-art, water-processable, recyclable radio frequency communication antennas.

4. Experimental Section

Materials: Graphite powders were purchased from Kibaran Resources Limited and used as received. This material is an air-classified powder with a stated D90 of 50 μm . Triton X-100 (Laboratory grade) was purchased from Sigma Aldrich and used as-received. Deionised water with a resistivity of 18.2 M Ω cm was prepared using a Thermo Scientific Barnstead MicroPure system. Powders of MoS₂, WS₂, BN, and MoSe₂ were purchased from Sigma Aldrich and used as-received. WSe₂ powder was purchased from ABCO Materials and used as received.

In a typical exfoliation process graphite powder was added to a pre-mixed solution of Triton X-100 in deionised water (4 g L^{-1}) at a mass content of 60 g L^{-1} . The dispersion was homogenized in 0.5 L batches to minimize sedimentation, using the optimized process parameters of 35 kPSI operating pressure, 20 $^{\circ}\text{C}$ chiller temperature, and ≈ 16 recirculation passes (each batch was processed for 30 min under continuous recirculation at a rate of 220 s L^{-1} pass^{-1}). For the other materials, the starting concentration of the bulk crystallite was fixed, and the surfactant concentration weighted by the ratio of densities of the bulk crystals (so that the approximate volume ratio of surfactant to crystallite remains constant).

Methods–Homogenization: Homogenization of surfactant dispersions was performed using a BEE International Mini DeBEE high-pressure homogenizer, with a D5 diamond nozzle (≈ 100 μm aperture), in a reverse flow configuration. The system heat exchanger was connected to an Applied Thermal Control Ltd K4 4.5 kW recirculating chiller, with temperature control between 5 and 35 $^{\circ}\text{C}$. During processing the thermal set point of the system was maintained to within 0.5 $^{\circ}\text{C}$.

Methods–Centrifugation: Centrifugation of homogenized dispersions was performed using a Beckman Coulter Avanti J15-R benchtop centrifuge with a JS-4750 swinging bucket rotor with maximum 3 L capacity (4×750 mL polypropylene centrifuge tubes).

Methods–UV–Vis Spectrophotometry: Spectroscopy of dispersions was performed in fused quartz 10 mm path length cuvettes (Starna Scientific) using a Shimadzu UV3600 Plus UV–vis–NIR spectrometer.

Methods–Dynamic Light Scattering: DLS measurements of hydrodynamic radius for size-selected dispersions were performed using an Anton Paar LiteSizer 500. The hydrodynamic radius measured was converted to a mean lateral nanosheet length using the equation;^[15]

$$L = 0.07 D^{1.5} \quad (3)$$

Methods–Raman Spectroscopy: A sample was prepared drop casting the graphene dispersion on silicon wafer. The wafer was heated above the boiling point of the solvent to remove any residual solvent. The non-resonant map

was taken using a Renishaw inVia Raman microscope with an excitation laser wavelength of 532 nm and a 2400 l mm⁻¹ grating. Step size was 0.3 μm in a square area of 20 μm side, 0.2 s as integration time per point, power of 5 mV and optical magnification of 100x.

Methods—Scanning Electron Microscopy: SEM imaging was performed with a Zeiss SIGMA field emission gun scanning electron microscope (FEG-SEM) using a Zeiss in-lens secondary electron detector. The FEG-SEM working conditions used were; 2.5 kV accelerating voltage, 20 μm aperture, and 2 mm working distance.

Methods—Atomic Force Microscopy: AFM was performed using a Bruker Dimension Icon instrument in Quantitative Nanomechanics (QNM) mode with a ScanAsyst-Air silicon nitride probe.

Methods—Sheet Resistance: Sheet resistances were measured using the transmission line approach. A series of parallel bars were painted onto the sample using Agar Scientific G302 Silver paint, such that their width, *W*, and adjacent separation, *L*, were equal. The two-point resistances between pairs of bars were measured with a Rapid Electronics 318 DMM digital multimeter, and recorded according to the bar separation in units of L W⁻¹. The gradient of the resulting graph (as shown in Figure 3A) gives the sheet resistance, with the y-intercept additionally giving the contact resistance.

Methods—Film Thickness: Film thicknesses were measured using the scratch depth technique. Films on substrate were scratched with a PTFE stylus and the depth of the scratch measured using the optically-encoded sample stage of a Renishaw inVia Raman microscope (with 100 nm position resolution and repeatability).

Methods—Thermogravimetric analysis: TGA measurements were performed to assess surfactant contents of dried materials using a TA Instruments TGA Q500. Samples were prepared by drying dispersions onto a silicone-coated release paper before being transferred to a platinum TGA pan. The samples were measured in air from room temperature to 900 °C at a ramp rate of 10 °C min⁻¹.

Methods—Screen Printing: Screen printing screens were prepared in house using Speedball Diazo Photo emulsion and 32T silk screen on an A3 wooden frame. After drying the emulsion was exposed through a printed transparency mask using a 2500 lumen LED bulb until the exposed areas were cured. The screen was then washed with a pressurized jet of tap water to remove the masked areas, revealing the screen pattern.

COG ink was prepared from centrifuge paste (produced as illustrated in Figure 3G) by dilution with ethylene glycol (purchased from Sigma Aldrich and used as-received), and placed onto the screen and dragged across it with a polyurethane-bladed squeegee to deposit the ink through the exposed mesh areas.

Methods—Optical Microscopy: Optical micrographs were captured using an Olympus BX53M optical microscope fitted with a 4K digital CCD camera.

Methods—Simulation of Antenna Response: Antenna designs were simulated using CST Microwave Studio.

Methods—Return Loss Measurements of Printed Antennae: Antennae were prepared on poly(ethylene terephthalate) (PET) substrates of 175 μm thickness purchased from Goodfellow Cambridge Ltd. Substrates were cleaned by wiping with lint-free tissues soaked in isopropanol prior to use. The antennas were punctured with an awl and a subminiature type A (SMA) right-angle connector was attached and connected to the antenna surface with Agar Scientific G302 silver paint.

Return loss measurements were made using a Pico Technology PicoVNA 106 Vector Network Analyzer (VNA), in single port mode using a 30 cm test lead. Prior to measurements the system was calibrated using a SOLT-STD-F calibration kit. Spectra were captured using ten-measurement-averaging over the range 100 kHz to 6 GHz.

Methods—RFID Tag Measurements: Measurements of tag switch on power and return power were made using an Impinj Speedway Revolution R120 UHF RFID reader.

Methods—Antenna Recycling: Antenna fragments were scraped from the substrate with a razor blade and added to a glass vial. DI water was added and the fragments were subjected to tip sonication using a Sonics Vibracell VCX130 for 10 min at 40% tip amplitude (<10 W output power). The resulting dispersion featured no visible aggregates or remaining

fragments (see Supporting Information), and was spray deposited back onto a PET substrate and the conductivity reassessed as previously described.

Supporting Information

Supporting Information is available from the Wiley Online Library or from the author.

Acknowledgements

The authors gratefully acknowledge support from Advanced Material Development Ltd in carrying out this work.

Conflict of Interest

The authors declare no conflict of interest.

Keywords

antennae, graphene, liquid-phase exfoliation, printing, scalability

Received: March 26, 2020

Revised: May 1, 2020

Published online: May 26, 2020

- [1] V. Nicolosi, M. Chhowalla, M. G. Kanatzidis, M. S. Strano, J. N. Coleman, *Science* **2013**, *340*, 1226419.
- [2] K. Parvez, R. Worsley, A. Alieva, A. Felten, C. Casiraghi, *Carbon* **2019**, *149*, 213.
- [3] I. H. Kim, T. Yun, J.-E. Kim, H. Yu, S. P. Sasikala, K. E. Lee, S. H. Koo, H. Hwang, H. J. Jung, J. Y. Park, H. S. Jeong, S. O. Kim, *Adv. Mater.* **2018**, *30*, 1803267.
- [4] Y. Hernandez, V. Nicolosi, M. Lotya, F. M. Blighe, Z. Sun, S. De, I. T. McGovern, B. Holland, M. Byrne, Y. K. Gun'Ko, J. J. Boland, P. Niraj, G. Duesberg, S. Krishnamurthy, R. Goodhue, J. Hutchison, V. Scardaci, A. C. Ferrari, J. N. Coleman, *Nat. Nanotechnol.* **2008**, *3*, 563.
- [5] K. R. Paton, E. Varrla, C. Backes, R. J. Smith, U. Khan, A. O'Neill, C. Boland, M. Lotya, O. M. Istrate, P. King, T. Higgins, S. Barwich, P. May, P. Puczkarski, I. Ahmed, M. Moebius, H. Pettersson, E. Long, J. Coelho, S. E. O'Brien, E. K. McGuire, B. M. Sanchez, G. S. Duesberg, N. McEvoy, T. J. Pennycook, C. Downing, A. Crossley, V. Nicolosi, J. N. Coleman, *Nat. Mater.* **2014**, *13*, 624.
- [6] P. G. Karagiannidis, S. A. Hodge, L. Lombardi, F. Tomarchio, N. Decorde, S. Milana, I. Goykhman, Y. Su, S. V. Mesite, D. N. Johnstone, R. K. Leary, P. A. Midgley, N. M. Pugno, F. Torrisi, A. C. Ferrari, *ACS Nano* **2017**, *11*, 2742.
- [7] A. E. Del Rio Castillo, V. Pellegrini, A. Ansaldo, F. Ricciardella, H. Sun, L. Marasco, J. Buha, Z. Dang, L. Gagliani, E. Lago, N. Curreli, S. Gentiluomo, F. Palazon, M. Prato, R. Oropesa-Nuñez, P. S. Toth, E. Mantero, M. Crugliano, A. Gamucci, A. Tomadin, M. Polini, F. Bonaccorso, *Mater. Horiz.* **2018**, *5*, 890.
- [8] S. Bellani, E. Petroni, A. E. Del Rio Castillo, N. Curreli, B. Martín-García, R. Oropesa-Nuñez, M. Prato, F. Bonaccorso, *Adv. Funct. Mater.* **2019**, *29*, 1807659.
- [9] W. Primak, L. H. Fuchs, *Phys. Rev.* **1954**, *95*, 22.

- [10] S. P. Ogilvie, M. J. Large, M. A. O'Mara, P. J. Lynch, C. L. Lee, A. A. K. King, C. Backes, A. B. Dalton, *2D Mater.* **2019**, *6*, 031002.
- [11] U. Khan, A. O'Neill, M. Lotya, S. De, J. N. Coleman, *Small* **2010**, *6*, 864.
- [12] C. Backes, K. Paton, D. Hanlon, S. Yuan, M. Katsnelson, J. Houston, R. Smith, D. McCloskey, J. Donegan, J. N. Coleman, *Nanoscale* **2016**.
- [13] P. Tiwari, N. Kaur, V. Sharma, S. M. Mobin, *Phys. Chem. Chem. Phys.* **2018**, *20*, 20096.
- [14] C. Backes, D. Campi, B. M. Szydłowska, K. Synnatschke, E. Ojala, F. Rashvand, A. Harvey, A. Griffin, Z. Sofer, N. Marzari, J. N. Coleman, D. D. O'Regan, *ACS Nano* **2019**, *13*, 7050.
- [15] M. Lotya, A. Rakovich, J. F. Donegan, J. N. Coleman, *Nanotechnology* **2013**, *24*, 265703.
- [16] P. He, J. Cao, H. Ding, C. Liu, J. Neilson, Z. Li, I. A. Kinloch, B. Derby, *ACS Appl. Mater. Interfaces* **2019**, *11*, 32225.
- [17] X. Huang, T. Leng, X. Zhang, J. C. Chen, K. H. Chang, A. K. Geim, K. S. Novoselov, Z. Hu, *Appl. Phys. Lett.* **2015**, *106*, 203105.
- [18] X. Huang, T. Leng, T. Georgiou, J. Abraham, R. Raveendran Nair, K. S. Novoselov, Z. Hu, *Sci. Rep.* **2018**, *8*, 43.
- [19] K. Pan, Y. Fan, T. Leng, J. Li, Z. Xin, J. Zhang, L. Hao, J. Gallop, K. S. Novoselov, Z. Hu, *Nat. Commun.* **2018**, *9*, 5197.
- [20] T. Leng, K. Pan, Y. Zhang, J. Li, S. Afroj, K. S. Novoselov, Z. Hu, *ACS Appl. Nano Mater.* **2019**, acsanm.9b01034.
- [21] C. Backes, B. M. Szydłowska, A. Harvey, S. Yuan, V. Vega-Mayoral, B. R. Davies, P. Zhao, D. Hanlon, E. J. G. Santos, M. I. Katsnelson, W. J. Blau, C. Gadermaier, J. N. Coleman, *ACS Nano* **2016**, *10*, 1589.
- [22] RFID Journal, <https://www.rfidjournal.com/faq/show?62> (Accessed: October 2019).